

NEW OBSERVATIONAL EVIDENCE OF ACTIVE ASTEROID P/2010 A2: SLOW ROTATION OF THE LARGEST FRAGMENT

YOONYOUNG KIM, MASATERU ISHIGURO, AND MYUNG GYOON LEE

Department of Physics and Astronomy, Seoul National University, Gwanak, Seoul 151-742, Korea
yoonyoung@astro.snu.ac.kr, ishiguro@astro.snu.ac.kr

Draft version October 11, 2018

ABSTRACT

We report new observations of the active asteroid P/2010 A2 taken when it made its closest approach to the Earth (1.06 au in 2017 January) after its first discovery in 2010. Despite a crucial role of the rotational period in clarifying its ejection mechanism, the rotational property of P/2010 A2 has not yet been studied due to the extreme faintness of this tiny object (~ 120 m in diameter). Taking advantage of the best observing geometry since the discovery, we succeed in obtaining the rotational light curve of the largest fragment with Gemini/GMOS-N. We find that (1) the largest fragment has a double-peaked period of 11.36 ± 0.02 hr spinning much slower than its critical spin period; (2) the largest fragment is a highly elongated object ($a/b \geq 1.94$) with an effective radius of $61.9_{-9.2}^{+16.8}$ m; (3) the size distribution of the ejecta follows a broken power law (the power indices of the cumulative size distributions of the dust and fragments are 2.5 ± 0.1 and 5.2 ± 0.1 , respectively); (4) the mass ratio of the largest fragment to the total ejecta is around 0.8; and (5) the dust cloud morphology is in agreement with the anisotropic ejection model in Kim et al. (2017). These new characteristics of the ejecta obtained in this work are favorable to the impact shattering hypothesis.

Subject headings: minor planets, asteroids: individual (P/2010 A2)

1. INTRODUCTION

P/2010 A2 (hereafter A2) is one of the main-belt asteroids receiving the most attention from Solar System scientists because of the mysterious dust ejection within the snow line of the Solar System (Jewitt et al. 2015). It was discovered on 2010 January 6, exhibiting a comet-like dust trail (Birtwhistle et al. 2010). Early analyses of its trail position angle indicated that the mass was impulsively ejected by either impact or rotational instability (Jewitt et al. 2010; Snodgrass et al. 2010). More detailed studies through dust-modeling analysis have suggested several different mechanisms (rotational breakup, impact cratering or shattering; Agarwal et al. 2013; Kleyna et al. 2013; Kim et al. 2017). Meanwhile, the characteristics of the fragments such as the rotation, shape, and size distribution have not been studied due to the extreme faintness of this tiny object (~ 120 m in diameter). Specifically, the rotational period of the largest fragment (LF) is critically important in clarifying the ejection mechanism of the active asteroid (Jewitt et al. 2015).

Here, we report new observations of A2 taken when it made its closest approach to the Earth after its discovery in 2010 (i.e., the geocentric distance $\Delta=1.06$ au in 2017 January). Since small dust particles, which enclosed the fragments in the images of the early 2010 observations (cf. Agarwal et al. 2013), have been swept away by solar radiation pressure over the eight years leaving behind a simple rod-shaped dust cloud, the new observation provides a more reliable data set for characterizing the fragment sizes. We utilized the golden opportunity to obtain the rotational light curve as well as the size distribution of the fragments. As a result, we have obtained the first evidence for the rotational status of the LF. In addition, we detected 10 possible sub-fragments. Based on the observational evidence, we consider the question of the

cause of the mass ejection from the asteroid.

2. OBSERVATIONS

We observed A2 for two successive nights on UT 2017 January 27–28 using the 8.1 m Gemini North telescope on Mauna Kea in Hawaii, as part of the Korean priority visiting program. Images were taken with the Gemini Multi-Object Spectrograph (GMOS; Hook et al. 2004) with a Sloan Digital Sky Survey (SDSS) g' -band filter, which is the most sensitive to the signal from A2 but less sensitive to sky background among the available filters. The image scale and the field of view are $0''.1454$ pixel⁻¹ and $5'.5 \times 5'.5$, respectively. Through test exposures, we identified the LF by comparing two individual images but noticed that it was $2''.72$ away from the position estimated by the JPL Horizons online ephemeris generator. We adjusted the position prior to the main observation. The non-sidereal rate of motion was sufficiently accurate that the telescope tracked the object adequately. The seeing was $\sim 0''.8$, and the weather was photometric during the observations. Observational data comprising a series of 300-second exposures were obtained on each night, giving 7.5 hr of total effective exposure time (Table 1). The point-like LF and surrounding dust cloud were clearly seen even in the individual images.

3. ANALYSIS AND RESULTS

3.1. Rotation, Shape, and Size of the Largest Fragment

We obtained photometry of the LF in each image using a circular aperture of projected radius $1''.3$. The sky background was determined within a concentric annulus with projected inner and outer radii of $1''.7$ and $3''.2$, respectively. Flux calibration was performed using Landolt standard stars (PG0231+051 and PG1047+003) at similar airmass to A2, while ~ 20 field stars in each individual image were also measured for differential photometry and

TABLE 1
OBSERVATION SUMMARY

UT Date and Time ^a	N^b	t^c	ν^d	r_h^e	Δ^f	α^g	θ_{-S}^h	θ_{-V}^i	δ_{\oplus}^j
2017 Jan 27 10:38–13:19	30	9000	29.3	2.034	1.057	5.0	119.0	286.5	-1.1
2017 Jan 28 06:11–10:49	50	15000	29.6	2.034	1.059	5.4	117.0	286.4	-1.0
2017 Jan 28 12:18–13:09	10	3000	29.6	2.034	1.060	5.5	116.6	286.3	-1.0

- ^a UT date and range of start times of the integrations.
^b Number of exposures.
^c Total exposure time, in seconds.
^d True anomaly, in degrees.
^e Heliocentric distance, in au.
^f Geocentric distance, in au.
^g Phase (Sun–target–observer’s) angle, in degrees.
^h Position angle of the antisolar vector, in degrees.
ⁱ Position angle of the negative heliocentric velocity vector, in degrees.
^j Angle of Earth above the orbital plane, in degrees.

used to correct for time-variable atmospheric extinction during each night. We converted the apparent magnitudes to absolute magnitudes (i.e., the magnitude at a hypothetical point at unit heliocentric and geocentric distances and at a zero Sun–asteroid–observer’s angle, the so-called phase angle) by

$$H_{g'} = m_{g'} - 5 \log_{10}(r_h \Delta) + 2.5 \log_{10}(\Phi(\alpha)), \quad (1)$$

in which r_h is the heliocentric distance. $\Phi(\alpha)$ is the phase function at solar phase angle α , where we used the H-G formalism with a slope parameter of $G = 0.25$ for S-complex asteroids (Bowell et al. 1989), which are dominant in the inner main-belt. Figure 1 shows the light curves of the LF measured from each image during our observations. To determine the periodicity in the light curve, we applied the phase dispersion minimization (PDM; Stellingwerf 1978) algorithm using the PDM package in IRAF and obtained the single-peaked period of $P_0 = 5.68 \pm 0.01$ hr. Other possible periods are multiples of P_0 , depending on the number of peaks appearing in one periodic phase. The maximum peak-to-peak amplitude was $\Delta m = 0.72 \pm 0.10$, where such large modulation is expected from a double-peaked light curve caused by an elongated shape (Harris et al. 2014). Assuming that the light curve results from an rotating triaxial ellipsoidal body having the axis ratio of $a : b : c$ ($a \geq b \geq c$), we obtained a double-peaked period of $P_{\text{rot}} = 2P_0 = 11.36 \pm 0.02$ hr and a lower limit on the axis ratio of $a/b = 10^{0.4\Delta m} \sim 1.94$. Earlier determinations of the absolute magnitudes in B , V , and R filters were $H_B = 22.77 \pm 0.02$, $H_V = 22.00 \pm 0.07$, and $H_R = 21.41 \pm 0.03$ (Jewitt et al. 2010, 2013). We used transformation equations between the Johnson-Cousins ($UBVRI$) system and the SDSS ($u'g'r'i'z'$) system (Smith et al. 2002), $g' = V + 0.54(B - V) - 0.07$, and obtained the corresponding absolute magnitude in the g' band, $H_{g'} = 22.34 \pm 0.07$ for $(B - V) = 0.77$, in agreement with the rotationally averaged magnitude from our photometry ($H_{g'} = 22.24 \pm 0.03$). The resulting absolute magnitude is converted into the effective radius (r_e) by the following equation (Russell 1916):

$$p_{g'} r_e^2 = 2.24 \times 10^{22} 10^{0.4(m_{\odot} - H_{g'})} \quad (2)$$

where $m_{\odot} = -26.37$ is the apparent solar g' -band magnitude (Blanton & Roweis 2007). Assuming a geometric g' -band albedo with large uncertainty, $p_{g'} = 0.21 \pm 0.08$,

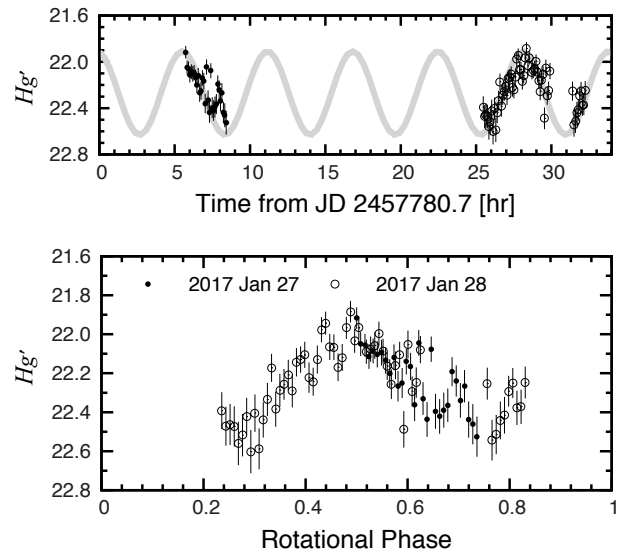


FIG. 1.— The rotational light curve of the LF. Time-series g' -band photometry over two nights (upper panel) and phase based on the best-fit double-peaked period of 11.36 hr (lower panel). A sine curve with a period of 11.36 hr was plotted in the upper panel (gray line). Two data points were excluded whose photometry was contaminated by field stars. The bump at rotational phase 0.6–0.7 is associated with neither contaminations of background sources nor data artifacts but can be indicative of rapidly changing cross-section due to a complicated shape.

corresponding to the average albedo of known S-complex asteroids (Usui et al. 2013; DeMeo & Carry 2013), we estimated an effective LF radius of $r_e = 61.9^{+16.8}_{-9.2}$ m. Using the r_e value, we obtained $a \sim 86.2$ m and $b \sim 44.4$ m.

3.2. Size Distribution of the Fragments

A composite image of A2 constructed from all data listed in Table 1 is shown in Figure 2 (a), where background stars were removed. Several local enhancements along the trail were visible near the LF. To extract these fragments in the composite image, we first used an unsharp masking technique, subtracting the 11-pixel \times 11-pixel ($1''.6 \times 1''.6$) median-filtered image. The large-scale components including the dust trail structure and sky background were subtracted by this method, leaving fine-scale structures (mostly signals from fragments). This flattened image was used for the detection of the fragments. The positions of the fragments were identified using SExtractor (Bertin & Arnouts 1996), and each sig-

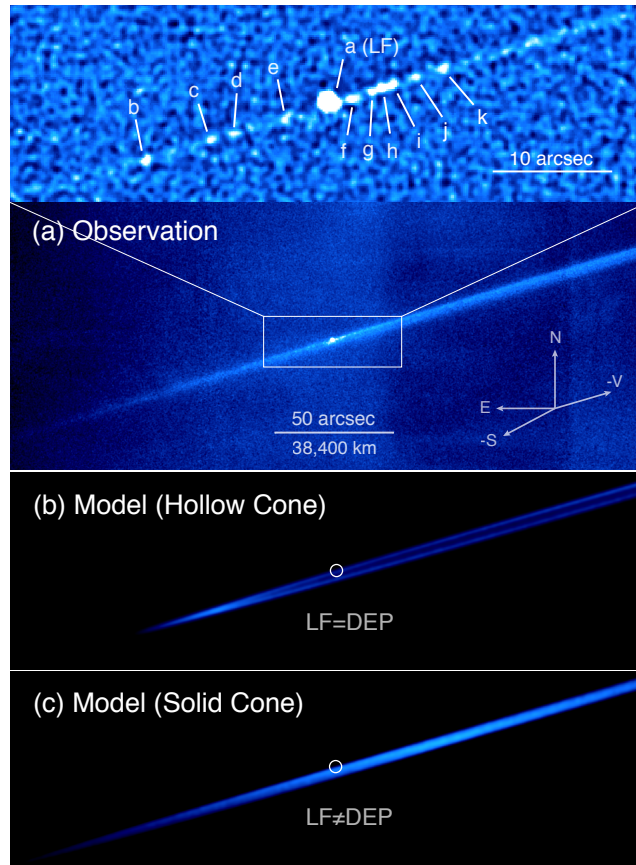


FIG. 2.— (a) Composite image of A2 constructed from all data listed in Table 1 (lower panel), where a box marks the region shown in the upper panel processed by subtracting the $11\text{-pixel} \times 11\text{-pixel}$ ($1''.6 \times 1''.6$) median image. We applied Gaussian smoothing to enhance the visibility of the fragments. Arrows show north (N), east (E), the projected negative heliocentric velocity vector ($-V$), and the antisolar direction ($-S$). (b) Model image of A2 assuming a hollow cone of dust as expected from an impact cratering (Ishiguro et al. 2011). The position of the LF is indicated by open circles, and the dust ejection point (DEP) is fixed to be the LF. (c) Model image of A2 assuming anisotropic ejection within a solid cone-shaped jet (Kim et al. 2017). In this model, we do not show the positions of the DEP because they exist beyond the field of view. The model images have the same image scale as the observation image, and we applied Gaussian smoothing to match the $0''.8$ seeing of the data.

nal in the original composite image was examined with the *APPHOT* package in IRAF for aperture photometry. To minimize the contaminating signals from nearby dust and fragments, we employed a small aperture of projected radius $0''.5$ and obtained their magnitudes in comparison with the LF measured using the same aperture radius. Finally, we selected the point-like sources with signal-to-noise ratios greater than 3 and confirmed 10 sub-fragments as well as the LF. The fragments detected by this technique are indicated in Figure 2 (a). The resulting apparent magnitudes of the sub-fragments were converted to absolute magnitudes and effective radii using Equation 1 and 2, respectively. For the LF, we adopted the rotationally averaged absolute magnitude and its effective radius from our light curve analysis (Section 3.1).

The cumulative size distribution of the fragments is shown in Figure 3 (filled circles), fitted with the dashed line with the power index of the cumulative size distribution, $q_S = 5.2 \pm 0.1$. We also show the size distribution of the dust cloud conjectured by means of a dust dynamical simulation (solid line). The power index of the dust cumulative size distribution was $q_S = 2.5 \pm 0.1$ (Jewitt et al. 2013; Kim et al. 2017), which is significantly shallower than that of the fragments. This discrepancy may suggest the nature of a broken power law distribu-

tion of the A2 ejecta. Similar trends are reported in the size distribution of boulders on asteroids (25143) Itokawa (Michikami et al. 2008) and those of collisional asteroid families (Zappalà et al. 2002) but are not clear in fragmented comets like 73P and 332P (Ishiguro et al. 2009; Jewitt et al. 2016).

The total dust mass was determined by previous research; that is, $M_d = (5\text{--}6) \times 10^8$ kg for the sizes < 0.2 m (Jewitt et al. 2013). We also obtained the consistent mass using the new observations through dust dynamical analysis (also see Section 4). Assuming the same mass density of the dust particles and fragments ($\rho = 3000$ kg m^{-3}), we estimated the mass of the LF and that of 10 sub-fragments as $M_{\text{LF}} = 3.0 \times 10^9$ kg and $M_{\text{sub}} = 1.7 \times 10^8$ kg, respectively. With the dust mass of $M_d = 6 \times 10^8$ kg, we obtained the mass ratio of the LF to the total ejecta (including the LF itself, 10 sub-fragments and dust), $M_{\text{LF}}/M_{\text{tot}} \sim M_{\text{LF}}/(M_{\text{LF}} + M_{\text{sub}} + M_d) \sim 0.8$.

4. DISCUSSION

Here, we consider possible ejection mechanisms of A2 based on the new characteristics of the fragments obtained in this work: (i) the slow rotation of the LF ($P_{\text{rot}} = 11.36$ hr), (ii) the highly elongated shape of

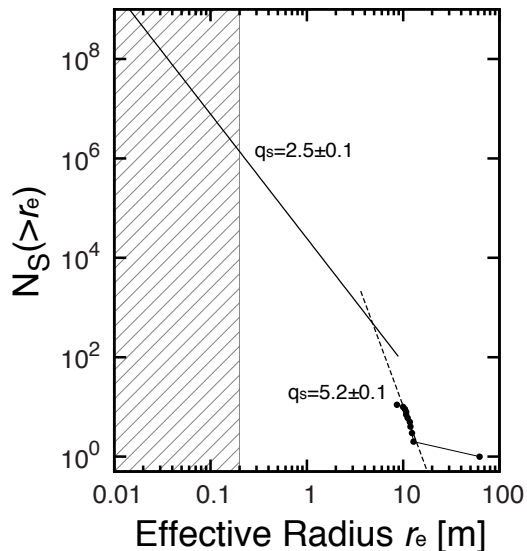


FIG. 3.— Cumulative size distribution of the dust particles and fragments measured in this work. Filled circles denote the fragments and are fitted to the line with the power index of the cumulative size distribution, $q_S = 5.2 \pm 0.1$ (dotted line). The shaded region denotes the dust particle regime (≤ 0.2 m), which is fitted to the line $q_S = 2.5 \pm 0.1$ (solid line).

the LF ($a/b \geq 1.94$), (iii) the effective LF radius ($r_e = 61.9$ m), and (iv) the large mass ratio ($M_{\text{LF}}/M_{\text{tot}} = 0.8$).

We start with the possibility of rotational instability. If an elongated object is spinning beyond the critical spin period, it is likely to shed surface materials at the ends of the longest axis where the strongest centrifugal force is exerted (Samarasinha et al. 2004; Hirabayashi & Scheeres 2014). Applying this scenario to the case of A2, the long axis of the precursor (a_0) is expected to be longer than that of the resultant LF (a_{LF}) after the mass ejection. Approximating the asteroid as a prolate ellipsoid whose mass is proportional to a under the same mass density ($M_{\text{tot}}/M_{\text{LF}} = a_0/a_{\text{LF}}$), the axis ratio of the precursor is estimated to be $(a/b)_0 = (M_{\text{tot}}/M_{\text{LF}})(a/b)_{\text{LF}} \sim 2.43$. Such highly elongated objects ($a/b > 2.4$) are extremely rare in the main asteroid belt but are present in some asteroid families (Szabó & Kiss 2008).

The rapid rotation of the primary body has been considered to be a key feature of rotationally disrupted asteroids. For a strengthless elongated body, the critical spin period for breakup (at which the gravitational acceleration equals the centripetal acceleration at the equator) is given by Jewitt (2012)

$$P_{\text{crit}} = (a/b)_0 \left[\frac{3\pi}{G\rho} \right]^{1/2}, \quad (3)$$

where $(a/b)_0 = 2.43$ is the axis ratio of the precursor and ρ is the mass density of the object. With $\rho = 3000 \text{ kg m}^{-3}$ for a monolithic precursor with a composition similar to S-complex asteroids, we obtained a critical spin period of $P_{\text{crit}} = 4.63$ hr. Alternatively, a slower critical spin period of $P_{\text{crit}} = 5.82$ hr can be obtained assuming a weak rubble pile precursor like (25143) Itokawa ($\rho = 1900 \text{ kg m}^{-3}$, Fujiwara et al. 2006).

It is reasonable to think that the spin period of the LF is constant after the mass ejection occurred in 2009 because YORP spin-down (Rubincam 2000) or relaxation

into the minimum rotational energy (Burns & Safronov 1973; Jewitt 2004) is not expected within the timescale of eight years. Although quantitative constraints on potential angular momentum loss during rotational breakup have not yet been studied (M. Hirabayashi 2017, private communication), we conjecture that it would be difficult to support the idea of the rotational breakup because the current spin period of the LF (11.36 ± 0.02 hr) is fairly longer than the P_{crit} . It is also noteworthy that other active asteroids whose ejection mechanism are presumed to be rotation-related, have revealed a rapid rotation close to their critical spin period (133P, 331P, and 62412; Hsieh et al. 2004; Drahus et al. 2015; Sheppard & Trujillo 2015).

Turning to the hypothesis of an impact cratering, we considered the potential crater size on the surface of the LF, based on the updated sizes and masses. Assuming that the LF lost its mass as the observed dust and 10 fragments through a cratering event where their mass density was the same ($\rho = 3000 \text{ kg m}^{-3}$), we obtained the total ejecta mass of $7.7 \times 10^8 \text{ kg}$ (cf. Section 3.2), corresponding to the total ejecta volume of $2.6 \times 10^5 \text{ m}^3$. The ejecta volume was set to be equal to the paraboloid crater volume $V = 1/3\pi R_c^3$, where we assume that the transient crater depth is a third of its diameter (Richardson et al. 2007). As a result, we obtained the crater radius of $R_c = 63$ m. The resulting crater radius on the surface of the LF is equivalent to the effective LF radius ($r_e = 61.9$ m), which is unlikely (cf. Hainaut et al. 2012). In addition, we conducted a model simulation of dust particles assuming a hollow cone of dust as expected from an impact cratering. The basic algorithm for the simulation is essentially the same as that described in Ishiguro et al. (2011), but appropriate model parameters were applied to reproduce the A2 dust cloud morphology (symmetric ejection with respect to a vector normal to the asteroid surface ($\alpha_{\text{cone}}, \delta_{\text{cone}}) = (30^\circ, -15^\circ)$ with a half-opening angle of $\theta = 35^\circ$ was assumed; cf. Kleyna et al. 2013). In the simulation image (Figure 2 (b)), the doublet structure associated with an impact cone would have been detected in the observed image. Although there are several solar system objects that have craters equivalent to the bodies' diameter (e.g., Mathilde and Deimos, Burchell & Leliwa-Kopystynski 2010), it is less probable that the mass ejection occurred at A2 through impact cratering because of the inconsistency of the morphology.

Most recently, Kim et al. (2017) suggested that the precursor asteroid was shattered by an impact and that remnants of slow “antipodal” ejecta were observed as the debris cloud of A2. We performed a model simulation of the dust particles and large fragments at the epoch of 2017 Gemini observation using the same algorithm and parameters in Kim et al. (2017). The model was found to be still suitable for our new observations, reproducing the dust cloud morphology and the trail surface brightness (Figure 2 (c)) as well as the positions of fragments (details in Kim et al. 2017). Additionally, we note that the slow rotation of the LF is in agreement with the impact shattering hypothesis; that is, laboratory impact experiments suggest that large or antipodal fragments tend to spin slowly (Fujiwara & Tsukamoto 1981; Nakamura et al. 1992).

While it is true that the large mass ratio of the LF to the total ejecta ($M_{LF}/M_{tot} = 0.8$) remains inconsistent with the impact shattering hypothesis, where the smaller mass ratio ($\lesssim 0.5$) is generally assumed (Holsapple et al. 2002), we strongly maintain that impact shattering is the likely mechanism of the activity of A2. Perhaps pre-existing fractures and voids in the precursor body enable the LF to be less damaged in the disruptive impact and maintain a larger mass, while a smaller M_{LF}/M_{tot} ratio can be obtained if we assume that the mass density of the dust particles is larger than that of the LF. If we consider the mass of invisible objects in the size range of 0.2–8 m, M_{tot} would increase. Therefore, M_{LF}/M_{tot} would be the upper limit. Although our new observations would not constitute conclusive evidence for the activity of A2,

they provide further evidence (slow rotation of the LF as well as the consistency of the anisotropic dust ejection model in Kim et al. (2017)) favorable to the hypothesis of impact shattering (i.e., catastrophic disruption).

We thank A. M. Nakamura, M. Hirabayashi, J. Āurech, D. Jewitt and the anonymous referee for their valuable comments. This work was supported by the National Research Foundation of Korea (NRF) funded by the Korean government (MEST; No. 2012R1A4A1028713) and the K-GMT Science Program (PID: GN-2016B-Q-14) of the Korea Astronomy and Space Science Institute (KASI). S.-C. Yang, H.-G. Lee and priority visitors helped with the Gemini observations.

REFERENCES

- Agarwal, J., Jewitt, D., & Weaver, H. 2013, *ApJ*, 769, 46
 Bertin, E., & Arnouts, S. 1996, *A&AS*, 117, 393
 Birtwhistle, P., Ryan, W. H., Sato, H., Beshore, E. C., & Kadota, K. 2010, *Central Bureau Electronic Telegrams*, 2114, 1
 Blanton, M. R., & Roweis, S. 2007, *AJ*, 133, 734
 Bowell, E., Hapke, B., Domingue, D., et al. 1989, *Asteroids II*, 524
 Burchell, M. J., & Leliwa-Kopystynski, J. 2010, *Icarus*, 210, 707
 Burns, J. A., & Safronov, V. S. 1973, *MNRAS*, 165, 403
 DeMeo, F. E., & Carry, B. 2013, *Icarus*, 226, 723
 Drahus, M., Waniak, W., Tendulkar, S., et al. 2015, *ApJ*, 802, L8
 Fujiwara, A., Kawaguchi, J., Yeomans, D. K., et al. 2006, *Science*, 312, 1330
 Fujiwara, A., & Tsukamoto, A. 1981, *Icarus*, 48, 329
 Hainaut, O. R., Kleyna, J., Sarid, G., et al. 2012, *A&A*, 537, A69
 Harris, A. W., Pravec, P., Galád, A., et al. 2014, *Icarus*, 235, 55
 Hirabayashi, M., & Scheeres, D. J. 2014, *ApJ*, 780, 160
 Hsieh, H. H., Jewitt, D. C., & Fernández, Y. R. 2004, *AJ*, 127, 2997
 Holsapple, K., Giblin, I., Housen, K., Nakamura, A., & Ryan, E. 2002, *Asteroids III*, W. F. Bottke Jr., A. Cellino, P. Paolicchi, and R. P. Binzel (eds), University of Arizona Press, Tucson, p.443-462, 443
 Hook, I. M., Jørgensen, I., Allington-Smith, J. R., et al. 2004, *PASP*, 116, 425
 Ishiguro, M., Hanayama, H., Hasegawa, S., et al. 2011, *ApJ*, 741, L24
 Ishiguro, M., Usui, F., Sarugaku, Y., & Ueno, M. 2009, *Icarus*, 203, 560
 Jewitt, D., Mutchler, M., Weaver, H., et al. 2016, *ApJ*, 829, L8
 Jewitt, D., Hsieh, H., & Agarwal, J. 2015, *Asteroids IV*, 221
 Jewitt, D., Ishiguro, M., & Agarwal, J. 2013, *ApJ*, 764, L5
 Jewitt, D. 2012, *AJ*, 143, 66
 Jewitt, D., Weaver, H., Agarwal, J., Mutchler, M., & Drahus, M. 2010, *Nature*, 467, 817
 Jewitt, D. C. 2004, *Comets II*, 659
 Kim, Y., Ishiguro, M., Michikami, T., & Nakamura, A. M. 2017, *AJ*, 153, 228
 Kleyna, J., Hainaut, O. R., & Meech, K. J. 2013, *A&A*, 549, A13
 Michikami, T., Nakamura, A. M., Hirata, N., et al. 2008, *Earth, Planets, and Space*, 60, 13
 Nakamura, A., Suguiyama, K., & Fujiwara, A. 1992, *Icarus*, 100, 127
 Richardson, J. E., Melosh, H. J., Lisse, C. M., & Carcich, B. 2007, *Icarus*, 190, 357
 Rubincam, D. P. 2000, *Icarus*, 148, 2
 Russell, H. N. 1916, *ApJ*, 43, 173
 Samarasinha, N. H., Mueller, B. E. A., Belton, M. J. S., & Jorda, L. 2004, *Comets II*, 281
 Sheppard, S. S., & Trujillo, C. 2015, *AJ*, 149, 44
 Smith, J. A., Tucker, D. L., Kent, S., et al. 2002, *AJ*, 123, 2121
 Snodgrass, C., Tubiana, C., Vincent, J.-B., et al. 2010, *Nature*, 467, 814
 Stellingwerf, R. F. 1978, *ApJ*, 224, 953
 Szabó, G. M., & Kiss, L. L. 2008, *Icarus*, 196, 135
 Usui, F., Kasuga, T., Hasegawa, S., et al. 2013, *ApJ*, 762, 56
 Zappalà, V., Cellino, A., dell’Oro, A., & Paolicchi, P. 2002, *Asteroids III*, 619